Since January 2020 Elsevier has created a COVID-19 resource centre with free information in English and Mandarin on the novel coronavirus COVID-19. The COVID-19 resource centre is hosted on Elsevier Connect, the company's public news and information website.

Biosensors and Bioelectronics 195 (2022) 113595

Contents lists available at ScienceDirect

Biosensors and Bioelectronics

journal homepage: www.elsevier.com/locate/bios

Aptamer-based electrochemical biosensor for rapid detection of SARS-CoV-2: Nanoscale electrode-aptamer-SARS-CoV-2 imaging by photo-induced force microscopy

Juan Carlos Abrego-Martinez [a], Maziar Jafari [a], Siham Chergui [a], Catalin Pavel [b], Diping Che [b], Mohamed Siaj [a,*]

[a] Department of Chemistry and Biochemistry, Université Du Québec à Montréal, Montréal, QC, H3C 3P8, Canada
[b] Azure Biosystems Canada, Montréal, QC, H4P 2N5, Canada

ARTICLE INFO

Keywords:
SARS-CoV-2
S-protein
Detection
Aptasensor
Photo-induced force microscopy

ABSTRACT

Rapid, mass diagnosis of the coronavirus disease 2019 (COVID-19) is critical to stop the ongoing infection spread. The two standard screening methods to confirm the severe acute respiratory syndrome coronavirus 2 (SARS-CoV-2) are polymerase chain reaction (PCR), through the RNA of the virus, and serology by detecting antibodies produced as a response to the viral infection. However, given the detection complexity, cost and relatively long analysis times of these techniques, novel technologies are urgently needed. Here, we report an aptamer-based biosensor developed on a screen-printed carbon electrode platform for rapid, sensitive, and user-friendly detection of SARS-CoV-2. The aptasensor relies on an aptamer targeting the receptor-binding domain (RBD) in the spike protein (S-protein) of the SARS-CoV-2. The aptamer immobilization on gold nanoparticles, and the presence of S-protein in the aptamer-target complex, investigated for the first time by photo-induced force microscopy mapping between 770 and 1910 cm^{-1} of the electromagnetic spectrum, revealed abundant S-protein homogeneously distributed on the sensing probe. The detection of SARS-CoV-2 S-protein was achieved by electrochemical impedance spectroscopy after 40 min incubation with several analyte concentrations, yielding a limit of detection of 1.30 pM (66 pg/mL). Moreover, the aptasensor was successfully applied for the detection of a SARS-CoV-2 pseudovirus, thus suggesting it is a promising tool for the diagnosis of COVID-19.

1. Introduction

The outbreak of the novel severe acute respiratory syndrome coronavirus 2 (SARS-CoV-2) in late 2019 led to the Coronavirus Disease 2019 (COVID-19) pandemic that has dramatically affected the public health and economic systems of the world (Pedersen and Ho, 2020; Shang et al., 2020). The SARS-CoV-2 has proven to be far more transmissible than the SARS-CoV and Middle East respiratory syndrome coronavirus (MERS-CoV) (Chen et al., 2020; Gerges-Harb et al., 2020; Li et al., 2021; Peeri et al., 2020), two similar coronaviruses (CoVs) that severely affect the respiratory system and that caused the outbreaks of SARS and MERS in 2003 and 2012, respectively (Gilbert, 2020; Guarner, 2020).

CoVs are enveloped viruses whose surfaces are heavily decorated with club-shaped glycosylated spike (S) structural proteins. Nucleocapsid (N), matrix (M) and envelope (E) proteins are the other major structural proteins that compose the CoVs (Kirtipal et al., 2020). The structure of the S-protein consists of three protomers, each containing the subunits S1 and S2, which are composed of 672 and 588 amino acids, respectively (Duan et al., 2020; Wrapp et al., 2020). The S1 subunit is of particular importance, since it contains the receptor binding domain (RBD) of the protein, which plays an essential role in the SARS-CoV-2 viral infection. It is now well known that the SARS-CoV-2 infects epithelial cells in the human respiratory system through the interaction between the RBD of the S-protein and the angiotensin-converting enzyme II (ACE2) expressed on host cells, while the S2 subdomain is required for membrane fusion (Duan et al., 2020; Shang et al., 2020; Sun et al., 2021; Wrapp et al., 2020). Additionally, the RBD determines the binding affinity to the host receptor, the specificity of the virus and the mortality rate (Cleri et al., 2020; Hussain et al., 2020; Luan et al., 2020). For these reasons, the S-protein is a key target for vaccine development and screening methods for COVID-19 detection. Despite the recently launched vaccines against COVID-19 (Wouters et al., 2021), the rapid

* Corresponding author. Université du Québec à Montréal, Département de chimie, 2101 Jeanne-Mance St., Montreal, QC, H2X 2J6, Canada.
E-mail address: siaj.mohamed@uqam.ca (M. Siaj).

https://doi.org/10.1016/j.bios.2021.113595
Received 17 June 2021; Received in revised form 15 August 2021; Accepted 25 August 2021
Available online 30 August 2021

spread of the multiple variants of the SARS-CoV-2 continues (Callaway and Ledford, 2021; Fontanet et al., 2021), therefore timely detection remains as crucial now as during the onset of the pandemic.

During the early stages of the COVID-19 outbreak, infected patients were correctly diagnosed through deoxyribonucleic acid (DNA) sequencing assays (Ji et al., 2020), nevertheless, the widespread use of this technology is not feasible, since it is expensive, time-consuming, and it must be performed under rigorous laboratory conditions by highly trained technicians. Reverse transcription polymerase chain reaction (RT-PCR) and serological tests (detection of antibodies) are the standard COVID-19 diagnostic techniques (Ji et al., 2020; Udugama et al., 2020); however, these assays are not without limitations. RT-PCR yields a relatively high rate of false-negative results, especially in the early stages of infection due to the low levels of SARS-CoV-2 RNA and the low detection sensitivity of the method (Ji et al., 2020; Tahamtan and Ardebili, 2020). In addition, several hours are needed to obtain a result (Long et al., 2020) and, although the cost of PCR assays is lower than DNA sequencing technology, it is relatively expensive for mass testing in most countries. On the other hand, serological tests are not meaningful for early diagnosis of COVID-19 due to the lengthy delay between infection and seroconversion (De Assis et al., 2021). Therefore, antibody tests are more reliable to identify past infection. Meanwhile, countless efforts pursued optimizing detection and diagnosis methods at point-of-care (POC) facilities and as self-detection kits, such as Lateral Flow Immunochromatographic Assay Strips (LFICS) for COVID-19 (Alpdagtas et al., 2020; Yüce et al., 2021). Unlike gene-targeting tests, the sensitivity of rapid immunochromatographic test (ICT) kits is dependent on the time past infection (Fujigaki et al., 2020). Mandatorily, 10–15 days past infection are essential to provide enough time for the viral immune-response to produce a measurable amount of IgM and IgG SARS-CoV-2 recognizing antibodies (Fujigaki et al., 2020). Thus, ICT assays are biased by delay time and can only provide a reliable diagnosis after a controlled environment quarantine period, although they are showing an increasing role as screening method due to their ease of use (Pegoraro et al., 2021).

Alternatively, biosensors could potentially be employed as diagnostic tools for COVID-19, since in general, they offer several advantages over conventional detection methods, such as rapid, selective, and low-cost detection over a wide range of analytes, including viruses (Bahadır and Sezgintürk, 2016; Mehrotra, 2016). Several groups have recently reported the development of biosensors for COVID-19, including devices targeting the RNA of SARS-CoV-2 (Zhao et al., 2021), and COVID-19 antibodies (Ali et al., 2021; Elledge et al., 2021; Yakoh et al., 2021; Zeng et al., 2020), as well as immunosensors targeting the spike and nucleocapsid proteins (Cerutti et al., 2020; Eissa and Zourob, 2021; Mavrikou et al., 2020). Nonetheless, short strands of oligonucleotides, known as aptamers, could also be employed as biorecognition elements for COVID-19 diagnosis, as they are able to recognize targets with high selectivity (Darmostuk et al., 2015) and possess advantages compared with immunosensors in terms of detection capabilities. For instance, aptamers are subjected to less steric hindrance on the surface of CoVs (65–125 nm in diameter) (Shereen et al., 2020) due to their smaller size, typically about 2–3 nm in diameter (30–60 nucleotides) in comparison with antibodies (12–15 nm in diameter) (Song et al., 2020). This, in theory, allows the binding of more recognition elements on the surface of the CoV, which leads to enhanced sensing performances. In addition, aptamers are stable in a wider range of temperature and pH and have lower production costs than antibodies (Darmostuk et al., 2015; Tombelli et al., 2005). For these reasons, we propose the use of an aptamer-based electrochemical biosensor for detection of SARS-CoV-2 S-protein. Song et al. recently identified two single-stranded (ss) DNA aptamer sequences with the ability to bind to the RBD of the SARS-CoV-2 (Song et al., 2020). Therefore, in this work, we employed one of those reported sequences to develop an aptamer-based sensing platform for impedimetric detection of SARS-CoV-2 S-protein. The immobilization of the ssDNA aptamer on gold nanoparticles (AuNPs) and the binding of S-protein with the aptamer were investigated through photo-induced force microscopy (PiFM) and electrochemical techniques. The resulting device exhibited excellent sensitivity and selectivity towards the SARS-CoV-2 S-protein and towards a SARS-CoV-2 pseudovirus, thus being a promising tool for COVID-19 detection.

2. Methodology

2.1. Reagents

The ssDNA aptamer sequence used in this work is a 51-nt 3-hairpin-structured aptamer targeting the SARS-CoV-2 RBD (K_d = 5.8 nM), recently reported by Song et al., (2020). The aptamer sequence, 5′-CAGCACCGACCTTGTGCTTTGGGAGTGCTGGTCCAAGGGCGTTAAT-GGACA-3′ with a 5′-Thiol C6 S–S modification (5/ThioMC6-D/) was supplied by Integrated DNA Technologies Inc. (Coralville, IA, USA).

The SARS-CoV-2 Spike RBD recombinant protein (51.5 kDa, Arg319-Phe541 expressed with the Fc region of mouse IgG1 at the C-terminus by HEK293 cells), SARS-CoV Spike protein (S1 Subunit, His Tag) and MERS-CoV Spike protein (S1 subunit, aa 1–725, His Tag) were purchased from SinoBiological, Inc.

Phosphate-buffered saline (PBS), sulfuric acid (H_2SO_4), potassium hydroxide (KOH), sodium nitrate ($NaNO_3$), and sodium chloride (NaCl) were purchased from Thermo Fischer. Potassium ferricyanide ($K_3[Fe(CN)_6]$), potassium ferrocyanide ($K_4[Fe(CN)_6]\cdot 3H_2O$), chloroauric acid ($HAuCl_4$), Tris-hydrochloride (Tris-HCl) and magnesium chloride ($MgCl_2$) were purchased from Sigma-Aldrich. All reagents were analytical grade and were used without further processing.

2.2. Development of aptasensor

Prior to the fabrication of the aptasensor, the duration of the potential pulse for AuNPs deposition, aptamer incubation time and target incubation time (Figs. S1, S2 and S3, respectively) were investigated using a glassy carbon electrode (GCE, BASi, 0.07 cm^2 area) in a typical 3-electrode cell with an Ag/AgCl (3 M NaCl) reference electrode (RE) and a Pt wire counter electrode (CE). The final sensing platform was therefore constructed with the optimum parameters for Au deposition time, aptamer incubation time and S-protein incubation time. Screen-printed carbon electrodes (SPCEs) purchased from BioDevice Technology were used for the development of the aptasensor. The SPCEs consisted of a carbon working electrode (WE) with an area of 0.026 cm^2, an Ag/AgCl reference electrode (E = 0.22 V vs. NHE) and a carbon counter electrode with a larger electroactive area than the WE. Prior to electrode modification, the working electrodes were electrochemically cleaned by cyclic voltammetry in 0.1 M H_2SO_4. Potential cycles between −1.5 V — 1.5 V vs Ag/AgCl were performed until obtaining a reproducible response. The electrodes where then washed with Nanopure™ water and dried with a jet of N_2. The electrochemical behavior of the cleaned electrodes was recorded in PBS solution containing 5 mM $[Fe(CN)_6]^{3-/4-}$. Next, the electrodes were immersed in a 5 mM $HAuCl_4$ + 0.1 M $NaNO_3$ solution and the electrodeposition of AuNPs onto SPCEs was performed through chronoamperometry by applying a potential pulse of −0.3 V vs Ag/AgCl during 840 s. The AuNPs-modified electrode surface was then cleaned employing a KOH exposure/potential sweep method reported by Heiskanen et al., (2008) which is well known to yield a highly clean Au surface (Fischer et al., 2009; Ho et al., 2019). Before proceeding to aptamer immobilization, 1.5 μM of disulfide-labeled ssDNA solution in binding buffer (BB, 50 mM Tris-HCl + 150 mM NaCl + 2 mM $MgCl_2$, pH = 7.5) was subjected to heating at 90 °C for 5 min, followed by cooling at −4 °C for 10 min for DNA renaturation. Finally, the solution was allowed to stand at room temperature for 5 min. Afterwards, 5 μL of aptamer solution was drop-casted onto the surface of the WE to immobilize the aptamer on the AuNPs via a self-assembled monolayer (SAM) (Oberhaus et al., 2020), which was spontaneously formed during incubation at 4 °C for 8 h. The aptamer-modified electrode was then gently rinsed with BB

to remove non-bound aptamer. The Aptamer/AuNPs/SPCE was subsequently incubated with 1 mM of 6-mercapto-1-hexanol (MCH) + 10 mM PBS solution for 30 min at room temperature to displace the non-specific adsorption of the aptamers and to block the non-modified Au area to avoid pinhole formation. A final rinsing step with BB was performed to remove non-bound molecules, thus obtaining the aptamer-based sensing probe. The development process and working principle of the aptasensor are illustrated in Scheme 1. A photograph of the fabricated device is shown in Fig. S4.

2.3. Characterization of the aptasensor

Cyclic voltammetry (CV) and electrochemical impedance spectroscopy (EIS) measurements were performed throughout every step of the sensor fabrication to follow the surface modification. Cyclic voltammograms were obtained in the potential range of [-0.4 — 0.7 V] at 50 mV s^{-1} scan rate, while EIS was recorded at a direct current (DC) potential of 0.11 V in the frequency range from 100 kHz to 100 mHz with a sinusoidal voltage perturbation of 10 mV amplitude, both acquired in 30 μL of PBS (pH = 7.4) solution containing 5 mM $[Fe(CN)_6]^{3-/4-}$ as redox probe. All electrochemical measurements were performed on a SP-300 potentiostat/galvanostat (Bio-Logic Science Instruments) controlled by EC-Lab® software, which was also employed for the fitting of the EIS data.

The morphology of AuNPs was studied by SEM with a JEOL JCM-6000 tabletop microscope operated at 15 kV.

Atomic force microscopy (AFM) and photo-induced force microscopy (PiFM) images of the modified electrode were captured with a VistaScope instrument (MolecularVista, San-Jose, USA). The probe was a gold-coated cantilever chip (Nanosensors, Neuchatel, Switzerland) with a tip diameter of ~10 nm. The microscope was coupled to a mid-infrared radiation source comprised of two quantum cascade lasers (QCLs), together spanning the 770–1910 cm^{-1} spectral range. The focused laser polarization was at 45°, partly *P*- and partly *S*-polarized. The *P*-polarized component dominated the PiFM signal. The elliptical irradiation spot size was roughly λ by 1.5 λ on the short and long axes of the ellipse respectively. The laser intensity was 0.1–1 W and the depth of the laser into the sample was 20 nm. 10-point PiF-IR line-spectra were recorded on 2 × 2 μm^2 topography scans of the AuNPs-modified SPCE, aptamer/AuNPs/SPCE and S-protein/Aptamer/AuNPs/SPCE at a rate of 30 s/spectrum, with ≤10 nm lateral surface resolution and with 0.5 cm^{-1} spectral resolution. The spectra were collected at a baseline intensity of 5.85% of the maximum available power in sideband mode. Each probed point was spaced out by 167 nm. PiFM mapping images were screened at different wavelengths between 770 and 1910 cm^{-1} with a scan speed of 1 line/second and with a 256-pixel resolution. Topography images were measured at the same speed and with the same pixel resolution.

2.4. Electrochemical detection of SARS-CoV-2 S-protein

5 μL of different concentrations (10 pM — 100 nM) of S-protein in PBS + 150 mM NaCl + 2 mM $MgCl_2$, (pH = 7.4) was drop-casted onto the sensing probe and incubated at room temperature for 40 min, followed by rinsing with BB to eliminate non-bound molecules. EIS measurements for detection were then acquired at a potential of 0.14 V in the frequency range from 100 kHz to 100 mHz with an amplitude of 10 mV in 30 μL of PBS solution containing 5 mM $[Fe(CN)_6]^{3-/4-}$.

The selectivity of the aptasensor was investigated using Spike proteins from SARS-CoV, MERS-CoV and SARS-CoV-2. The probe was separately incubated during 40 min with 10 nM of these analytes and the impedimetric response was then recorded in redox probe/PBS.

2.5. Electrochemical detection of SARS-CoV-2 pseudovirus

To assess the potential application of the aptasensor as a COVID-19 detection method, the device was incubated with 5 μL of a SARS-CoV-2 pseudovirus, kindly provided by Prof. Benoit Barbeau, Université du Québec à Montréal. The SARS-CoV-2 pseudovirus was produced by transfection of HEK293T cells with an Env-deficient HIV_{NL4-3} plasmid and a plasmid expressing SARS-CoV-2 Spike. Experiments with the HIV_{NL4-3} plasmid (no spike) were also performed as control. The concentration of the HIV_{NL4-3}Env-luc plasmid and the SARS-CoV-2 pseudovirus was 12294 cpm/μL, as measured by scintillation counter.

3. Results and discussion

3.1. Electrodeposition of AuNPs on SPCE

Fig. 1a displays the first and second cycle obtained by cyclic voltammetry with a SPCE in 5 mM $HAuCl_4$ + 0.1 M $NaNO_3$ solution. The

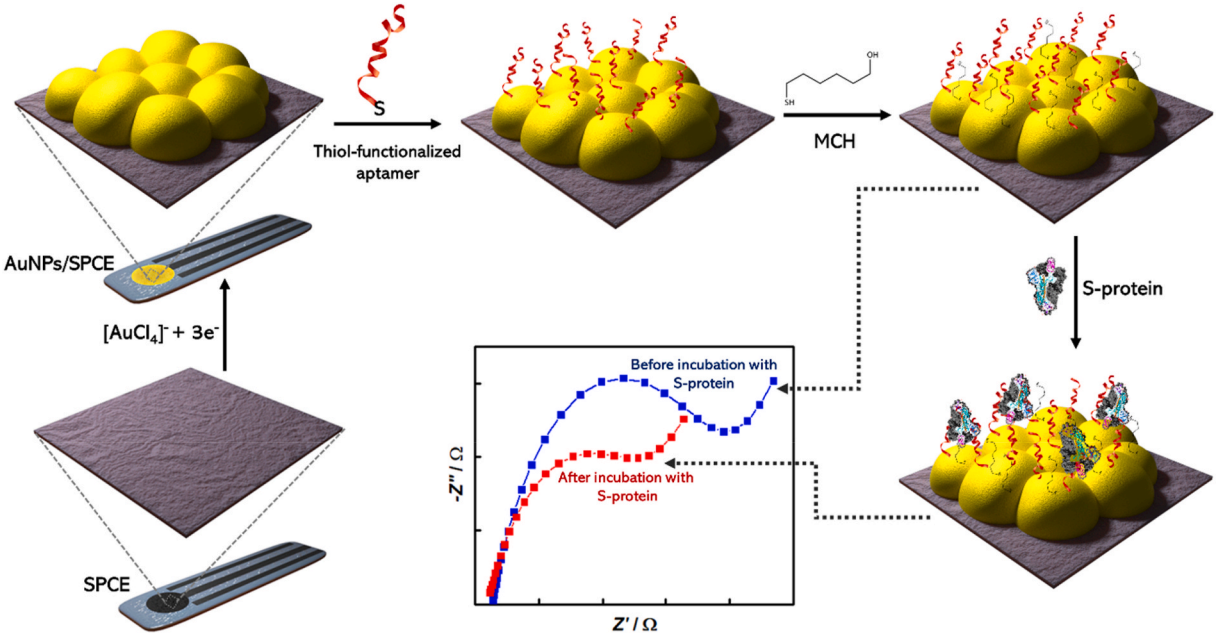

Scheme 1. Stepwise fabrication of aptasensor for SARS-CoV-2 S-protein detection.

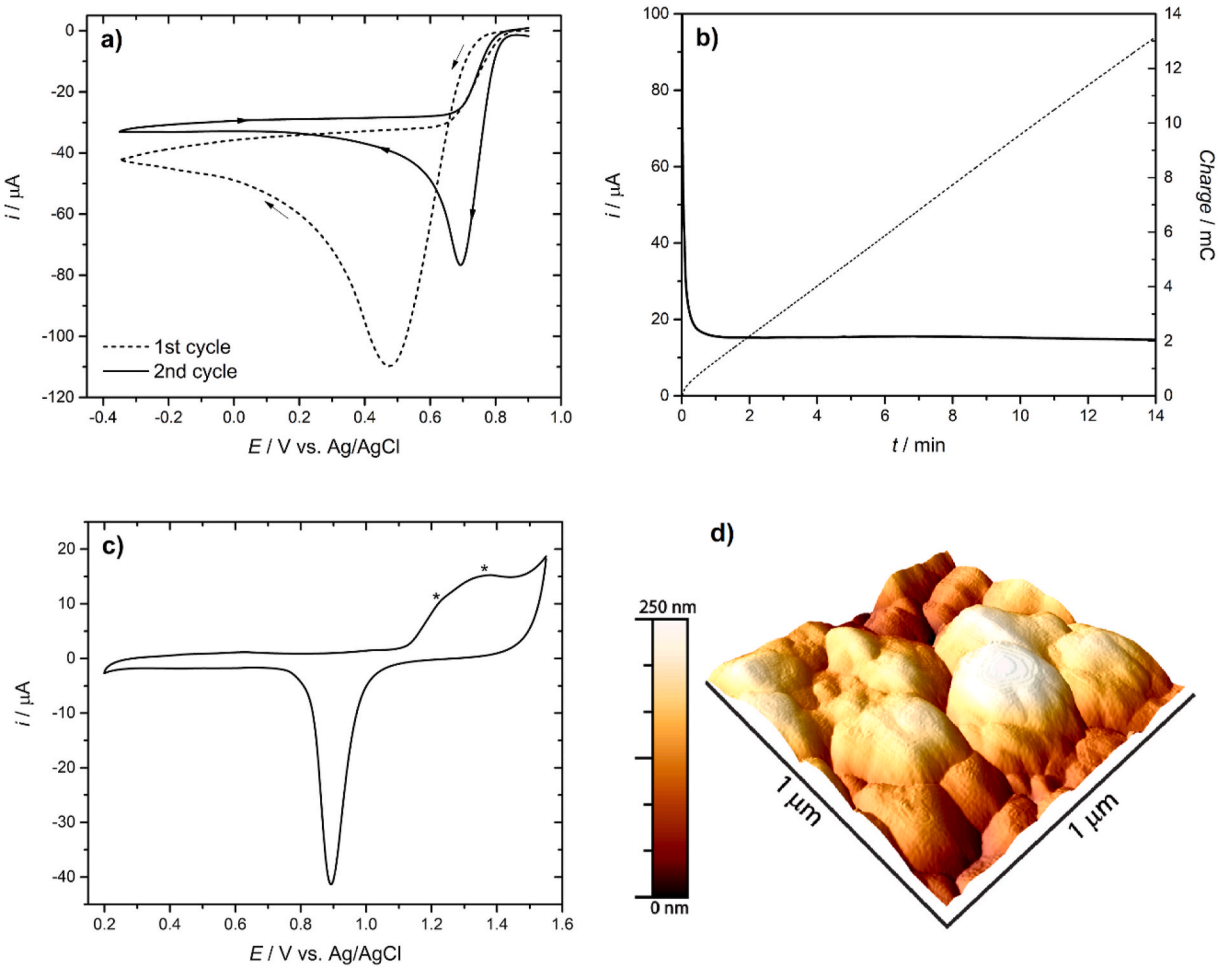

Fig. 1. a) CVs (first and second cycle) of Au(III) reduction at a SPCE recorded in 5 mM $HAuCl_4$ + 0.1 M $NaNO_3$ (50 mV s^{-1} scan rate), b) Current transient and charge consumed recorded during electrodeposition of AuNPs on a SPCE from a 5 mM $HAuCl_4$ + 0.1 M $NaNO_3$ solution, c) electrochemical profile of AuNPs/SPCE recorded in 0.5 M H_2SO_4 (50 mV s^{-1} scan rate), and d) three-dimensional AFM image of the AuNPs/SPCE.

first scan in the cathodic direction (dashed line) shows an increase of cathodic current starting at ≈0.75 V with a peak at 0.47 V, which is ascribed to the reduction of Au(III) to Au(0), according to (1):

$$AuCl_4^- + 3e^- \rightarrow Au + 4Cl^- \quad (1)$$

In the backward scan (anodic direction), a current crossover is observed at 0.65 V, which is a typical feature of nucleation on the electrode surface (Grujicic and Pesic, 2002; Inamdar et al., 2007). However, during the second cathodic scan (solid line), the Au(III) reduction peak shifted towards a less cathodic potential (0.7 V), indicating that the reduction of Au(III) occurs on the Au previously deposited. Therefore, under these conditions, electrodeposition of Au on the NPs deposited during the first scan is thermodynamically more favorable than nucleation of new AuNPs on the carbon electrode. Based on this CV, a potential of −0.3 V was applied to the working electrode through chronoamperometry for electrodeposition of AuNPs, since at this value the overpotential is large enough to favour the nucleation of new sites on the C electrode rather than the growth of previously established nuclei (Hezard et al., 2012). The potential pulse was applied during 840 s, according to the optimization reported in Fig. S1. The current transient presented in Fig. 1b exhibits a typical high current at very short times due to the charging of the double layer. Formation of initial nuclei also occurred at this early stage. Then, a current decay is observed until steady state is achieved, which corresponds to overlapping of the diffusion zones defined by each nucleus, as described by the Cottrell's equation (Grujicic and Pesic, 2002). According to the amount of charge consumed during chronoamperometry, a mass loading of 300 µg cm^{-2} of Au was electrodeposited on the electrode. The resulting AuNPs were electrochemically characterized by CV in 0.5 M H_2SO_4 in the potential range of [0.20 — 1.55 V]. The electrochemical profile, shown in Fig. 1c, exhibited a broad signal in the anodic scan between 1.15 and 1.40 V, that is rather the result of the contribution of two anodic peaks (marked with *) ascribed to the formation of different gold oxides, mainly AuO (Angerstein-Kozlowska et al., 1986; Hezard et al., 2012; Rouya et al., 2012; Tian et al., 2006), according to (2):

$$Au + H_2O \rightarrow AuO + 2H^+ + 2e^- \quad (2)$$

In the cathodic scan, a reduction peak was observed at 0.88 V, which corresponds to the reduction of gold oxides formed during the anodic scan. Therefore, the presence of Au deposited on the SPCE was confirmed. A top view SEM image of the AuNPs-modified surface is presented in Fig. S5, which shows hemispherical gold nanoparticles of about 250 nm diameter homogeneously distributed on the electrode. AFM was used to characterize the topography of the AuNPs deposited on the SPCE. The three-dimensional AFM image, shown in Fig. 1d exhibits nearly hemispherical aggregated nanoparticles of 250 — 300 nm diameter and a maximum of 250 nm in height, densely coating the surface of the electrode, which is consistent with the high overpotential applied and the long deposition time that allowed a continuous growth of the initial nuclei. The root-mean-square (RMS), indicative of the surface roughness, calculated from smaller 350 nm^2 area was 16.6 nm.

3.2. Electrode modification and PiFM characterization

The development of the sensing device was followed up by CV and EIS. Fig. 2a and b shows the cyclic voltammograms and Nyquist plots, respectively, obtained after every step of the aptasensor fabrication process. The Randles equivalent circuit used to fit the impedance data is displayed in the inset of Fig. 2b, and it consists of the solution resistance (R_s), the charge transfer resistance (R_{ct}), a constant phase element (CPE)

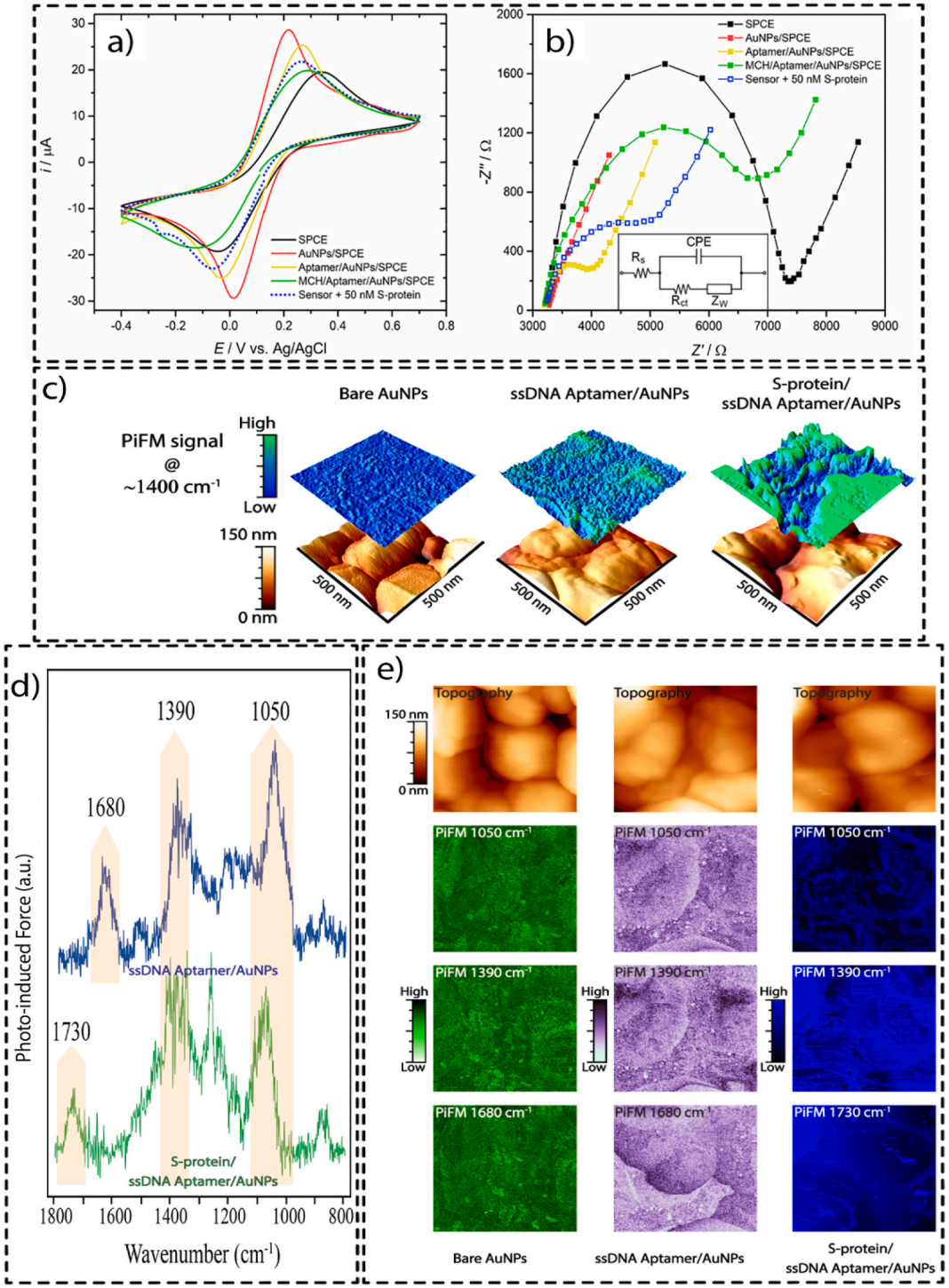

Fig. 2. a) CV and b) EIS measurements for every step of the aptasensor fabrication, recorded in PBS solution containing 5 mM $[Fe(CN)_6]^{3-/4-}$ (c–e) AFM and PiFM characterization of the modified electrode after each modification step. c) Three-dimensional topography and PiFM screening at ~1400 cm^{-1} representations of the AuNPs-, Aptamer/AuNPs- and S-protein/Aptamer/AuNPs-modified SPCEs. According to the PiF-IR spectra (Fig. 2d) and targeting selected peak shifts for best chemical contrast, the common wavenumbers at (~1050, ~1390 cm^{-1} and 1680–1730 cm^{-1}) were selected for PiFM mapping. d) Representative PiF-IR spectra acquired on the Aptamer/AuNPs- and S-protein/Aptamer/AuNPs-modified SPCEs, respectively in blue and green. Highlighted regions are mutual resonance peaks observed in both samples e) AFM and PiFM 500 × 500 nm^2 micrographs of the AuNPs-, Aptamer/AuNPs-and S-protein/Aptamer/AuNPs-modified SPCEs at the highlighted region wavenumbers in d), ~1050, ~1390 and ~1680-1730 cm^{-1}. (For interpretation of the references to colour in this figure legend, the reader is referred to the Web version of this article.)

which models the non-ideal behavior of the double layer capacitance, and a Warburg impedance element (Z_W). In all cases, 5 mM of $[Fe(CN)_6]^{3-/4-}$ solution was used as redox probe in PBS (pH = 7.4) as supporting electrolyte. The voltammogram obtained with the bare SPCE electrode exhibits the characteristic oxidation and reduction peaks of the redox couple at 0.34 V and −0.05 V, respectively, with a peak-to-peak separation (ΔE_p) of 390 mV, which is overall indicative of slow electron transfer rate. However, after electrodeposition of AuNPs, the ΔE_p value decreased to 189 mV, with anodic and cathodic peak currents of ≈29 μA, evidencing enhanced electron transfer kinetics on the gold surface. Following electrode incubation with the aptamer, an increase of ΔE_p to 306 mV was observed, as well as a decrease of both, anodic and cathodic peak currents (I_p), which indicates hindering of electron transfer, resulting from the electrostatic repulsion between the negatively charged aptamer and the redox couple (Fan et al., 2013; Mehennaoui et al., 2019) thus revealing aptamer immobilization on AuNPs. After incubation with MCH, the reduction peak further shifted towards cathodic potentials, while the oxidation peak slightly shifted to a more positive potential (ΔE_p = 415 mV) both with significantly lower current density, suggesting effective blockage of the nonspecific binding Au sites (Mehennaoui et al., 2019). However, the electrocatalytic activity was partially recovered upon incubation with 50 nM of S-protein, as observed in the peak-to-peak separation (ΔE_p = 323 mV) and higher peak current density. This consistently observed behavior can be ascribed to the positively charged nature of the S-protein (Hassanzadeh et al., 2020; Kucherova et al., 2020), which promotes an electrostatic attraction of the negatively charged $[Fe(CN)_6]^{3-/4-}$ redox probe in the solution, thus favouring the electron transfer rate.

Similarly, the Nyquist plots (Fig. 2b) show the stepwise electrode modification. For the bare SPCE, a semicircle corresponding to a charge transfer resistance of 3968 ohms was obtained. After AuNPs deposition, a semicircle as small as 20 ± 2 Ω was observed, implying very fast rate of charge transfer at the AuNPs surface. However, for the aptamer-modified electrode, the charge transfer resistance increased to 766 ± 16 Ω, caused by the electrostatic repulsion between the negatively charged aptamer layer and the $[Fe(CN)_6]^{3-/4-}$ redox couple (Fan et al., 2013; Mehennaoui et al., 2019), thus confirming the aptamer immobilization on the AuNPs. A further increase of the semicircle diameter (R_{ct} = 3693 ± 50 Ω) was observed after incubation of the electrode with MCH, as the presence of MCH on the Au surface blocks nonspecific binding and hinders the interfacial electron transfer (Mehennaoui et al., 2019). An additional EIS measurement was performed after incubating the aptamer probe with 50 nM of S-protein during 40 min. The resulting Nyquist plot exhibited a significant reduction of the charge transfer resistance in comparison with the measurement without analyte. This change in R_{ct} is product of the interaction between the positively charged S-protein and the negatively charged redox species in solution, which substantiates the effective formation of aptamer-target complex. EIS results were consistent with the observations through CV, which confirm the successful fabrication of the aptasensor. Furthermore, the analyte-induced change in charge transfer resistance demonstrates the working principle of this aptasensor and indicates that it can be employed to determine the presence of the S-protein of SARS-CoV-2.

The AFM three-dimensional images and chemical signatures obtained by PiFM of the modified SPCEs are also shown in Fig. 2. The topography images of the AuNPs, Aptamer/AuNPs and S-protein/Aptamer/AuNPs samples (Fig. 2c) revealed a visible decrease in the roughness of the electrode, from 16.6 nm to 12.3 nm upon aptamer binding, explained by the uniform formation of aptamer monolayer on the AuNPs. However, incubation of the aptamer probe with 50 nM of S-protein solution resulted in increased electrode surface roughness to 25.0 nm. Moreover, scattered grains *ca.* 15 nm in height were observed in an aggregated fashion atop the sample features (Fig. 2c and e). This profile is consistent with the height of the spike protein of the SARS-CoV and SARS-CoV-2 viruses (Neuman et al., 2006; Zhu et al., 2020). Given that the samples exhibited similar features in terms of NPs size and shape suggests that no major topography changes occurred as the electrode underwent modification. Fig. 2d shows the PiF-IR spectra (green and blue) of Aptamer/AuNPs- and S-protein/Aptamer/AuNPs-modified electrodes, respectively. In the 1500-1800 cm^{-1} region, known for the in-plane vibrations and double bond (C═C, C═N and C═O) stretching of the nucleic acid moieties, it was found that the initially observed ssDNA aptamer signal at ~1680 cm^{-1} experienced a hypsochromic shift to ~1730 cm^{-1} upon complexation with the viral spike protein (Wood, 2016). Stabilization of the ss nucleic acids when binding to the S-protein accounts for higher energy light absorption needed to promote the C = X bonds to energetically increasing vibrational states. On top of the sum of simultaneous specific non-covalent ligand-receptor interactions, being electron-rich molecules, nucleic acids are influenced by neighbouring π-π interactions that occur between aromatic residues of the S-protein and the ssDNA aptamer. This observation is fortified by the noticeable localized region of high intensity in the north-east corner of the PiFM map when scanning the S-protein/Aptamer/AuNPs modified SPCE at ~1730 cm^{-1}, highlighting an area of greater binding between ligand and receptor, in comparison to the rest of the scanned frame. Moreover, the uneven signal observed in the latter scan contrasts with the more uniformly distributed signal on the Aptamer/AuNPs-modified SPCE scanned at ~1680 cm^{-1} (Fig. 2e), evidencing a change in the chemistry of the ssDNA aptamer once the S-protein was bound. At this same wavenumber, no signal was observed on the bare AuNPs modified SPCE, in accordance with its acquired PiF-IR representative spectra (Fig. S6). As for the peak located in the ~1050 cm^{-1}, originating from the phosphate-backbone symmetric stretch of the ssDNA aptamer (Polito et al., 2021), no peak shift occurred. Fig. 2e shows the PiFM images taken at different wavelength (~1050, ~1390 cm^{-1} and 1680–1730 cm^{-1}) along with the corresponding AFM topography image. The PiF-IR spectra (Fig. 2d) of the samples revealed clear changes in their chemical signatures, including at around 1400 cm^{-1} (between 1350 and 1450 cm^{-1}) after incubation with S-protein. With this prospect, three-dimensional PiFM mapping images acquired at around 1400 cm^{-1} over an area of 500 × 500 nm^2 for all the samples (Fig. 2c) demonstrate morphology and spectroscopic signatures resulting from the interaction of the ssDNA aptamer and the SARS-CoV-2 S-protein. Compared to the bare AuNPs electrode, the PiFM signal at ~1400 cm^{-1} detected from the Aptamer/AuNPs sample arises from the DNA sugar-backbone/base bending modes, sensitive to glycosidic torsion angles (Parker and Quinn, 2013). Indeed, following incubation with S-protein, PiFM mapping showed that the signal intensified, densified, and appeared on larger zones of the sampled area (Fig. 2c). Peptide bonds, comprised of amide groups, resonate in the *ca.*1400 cm^{-1} region of the spectrum through the amide III vibration modes (Mallamace et al., 2015). Moreover, it was found that the PiFM mapping signal corresponded accurately to the morphology of the AuNPs-modified electrode, thus revealing abundant S-protein present in the aptamer-target complex homogeneously distributed on the sensing probe. Hence, the PiFM mapping images at ~1050 cm^{-1}, arising from the PO_2 ssDNA aptamer backbone vibrations, are consistent with this explanation (Fig. 2e). A lesser change is perceived between the Aptamer/AuNPs- and S-protein/Aptamer/AuNPs-modified SPCEs signal intensity distributions at this wavenumber. The subtle difference in the PiFM mapping images is perceived exclusively at the AuNP contours. A slight intensification in signal distribution on the AuNPs perimeters post-incubation with the S-protein, without any PiF-IR spectral peak shifts, confers a non-specific binding role to the PO_2 aptamer backbone toward the S-protein. Effectively, being positively charged, the S-protein is drawn to the phosphate groups by electrostatic forces, strengthening the ligand-receptor complex stability. In summary, as observed in Fig. 2c, the PiFM signal intensity distributions are null, uniform and locally elevated at ~1400 cm^{-1} due to negligeable resonance on the bare AuNPs, to medium resonance of the glycosidic backbone in the Aptamer/AuNPs- and to perceivable amide III resonance on the S-protein/Aptamer/AuNPs-modified SPCEs, respectively. The PiFM scans at ~1390 cm^{-1} in

Fig. 2e concur the latter observations. The ssDNA aptamer's nucleic acid resonance peak at ~1680 cm^{-1} undergoes a blue shift to ~1730 cm^{-1} after complexation with the S-protein, explained by ligand-receptor complex stabilization and electronic interactions. Finally, the detected aptamer PO_2-backbone symmetric stretching peak at ~1050 cm^{-1} remains invariable after the incubation with the S-protein, implying it contributes to non-specific electrostatic stabilization of the aptamer—S-protein complex.

3.3. Electrochemical detection of SARS-CoV-2 S-protein

The analytical performance of the aptasensor was investigated through EIS by measuring the changes in R_{ct} before and after 40 min incubation of the probe with different concentrations (0.01, 0.05, 0.10, 0.50, 1, 5, 10, 25, 50 and 100 nM) of S-protein. The resulting Nyquist plots are shown in Fig. 3a, along with the fitting curves calculated with the equivalent circuit shown in the inset of Fig. 2b. From the fitting it is observed that the charge transfer resistance exhibits a decreasing trend with increasing analyte concentration. The enhanced electron transfer is explained by the attraction between the positively charged S-protein on the probe and the negatively charged $[Fe(CN)_6]^{3-/4-}$ redox species in solution. This behavior therefore revealed that more S-protein is captured in the aptamer-target complex as the analyte concentration increases. The percentage change in charge transfer resistance ($\%\Delta R_{ct}$), defined as $[(R_0\text{-}R_{S\text{-protein}})/R_0] \times 100$, where R_0 and $R_{S\text{-protein}}$ are the R_{ct} before and after analyte binding, respectively, was calculated for each concentration and then plotted as a function of the S-protein concentration to construct the calibration curve, as displayed in Fig. 3b. Data points and error bars represent the average value and standard deviation from 3 independent measurements. The calibration curve of the aptasensor exhibits a linear relationship between the $\%\Delta R_{ct}$ and the S-protein concentration in a semi-logarithmic plot in the range of 10 pM — 25 nM, while the corresponding logarithmic regression equation is $\%\Delta R_{ct} = 32.1 + 14.9\ \log C[\text{nM}]$, ($R^2 = 0.9954$). From this response, the limit of detection (LOD) for SARS-CoV-2 S-protein was 1.30 pM (66 pg/mL), calculated as $3*(S_a/b)$, where S_a is the standard deviation of the response (determined by the standard deviation of y-intercept) and b is the slope of the calibration curve (Shrivastava and Gupta, 2011). This value is significantly lower than the LOD of ELISA for SARS-CoV-2 N-protein (0.4 ng/mL) (Eissa and Zourob, 2021) and for SARS-CoV-2 S-protein (0.7 ng/mL) (Lee et al., 2021), which highlights the excellent sensitivity of the aptasensor. A comparison of the analytical performance of this aptasensor and other detection methods for COVID-19 is summarized in Table S1.

3.4. Selectivity and stability of the aptasensor

Given the similarity between SARS-CoV, MERS-CoV and SARS-CoV-2 Spike proteins, the aptasensor was separately incubated in 10 nM of these analytes for 40 min and the impedimetric response was recorded to study the selectivity towards SARS-CoV-2 S-protein. The percentage change in charge transfer resistance relative to BB is displayed in Fig. 4a. While the response of the aptasensor towards MERS S-protein was only 7%, the device exhibited relatively high activity towards the SARS S-protein ($\%\Delta R_{ct}$ = 26%). This value represents more than half the response obtained with the SARS-CoV-2 S-protein (43%). This is not surprising, since the S-proteins of SARS-CoV and SARS-CoV-2 share a sequence identity of 77% (Hassanzadeh et al., 2020). However, despite the high sequence and structural similarity, the SARS-CoV-2 S-protein is slightly more positively charged than the SARS-CoV S-protein, which is one of the reasons why the former exhibits greater affinity to the ACE2 receptor that contributes to its transmission efficiency (Hassanzadeh et al., 2020). This difference in charge is likely to be the main differentiator in the behavior of the aptasensor towards SARS-CoV-2 and SARS-CoV S-proteins, which causes the former to be detected with more sensitivity. Since the SARS is considered eradicated in humans (Smith, 2019), a false positive result caused by SARS-CoV is unlikely.

To assess the stability of the aptamer probe, the impedimetric response of the aptasensor towards 50 nM SARS-CoV-2 S-protein was recorded after up to 3 weeks storage in BB at 4 °C and contrasted with the response obtained with the freshly fabricated device. The EIS measurements shown in Fig. 4b revealed that the R_{ct} increased from 1855 to 1872 Ω after 21 days, which represents a sensing activity loss of only 1% with respect to the fresh device. This result demonstrates that the aptamer probe is remarkably stable under the mentioned storage conditions, and it suggests that the aptasensor is capable of reliable detection up to 3 weeks after device fabrication.

3.5. Electrochemical detection of SARS-CoV-2 pseudovirus

To investigate the feasibility of practical application for COVID-19 detection, the aptasensor was tested with a pseudovirus consisting of $HIV_{NL4\text{-}3}$Env-luc + SARS-CoV-2 S-protein. Experiments with a spike-

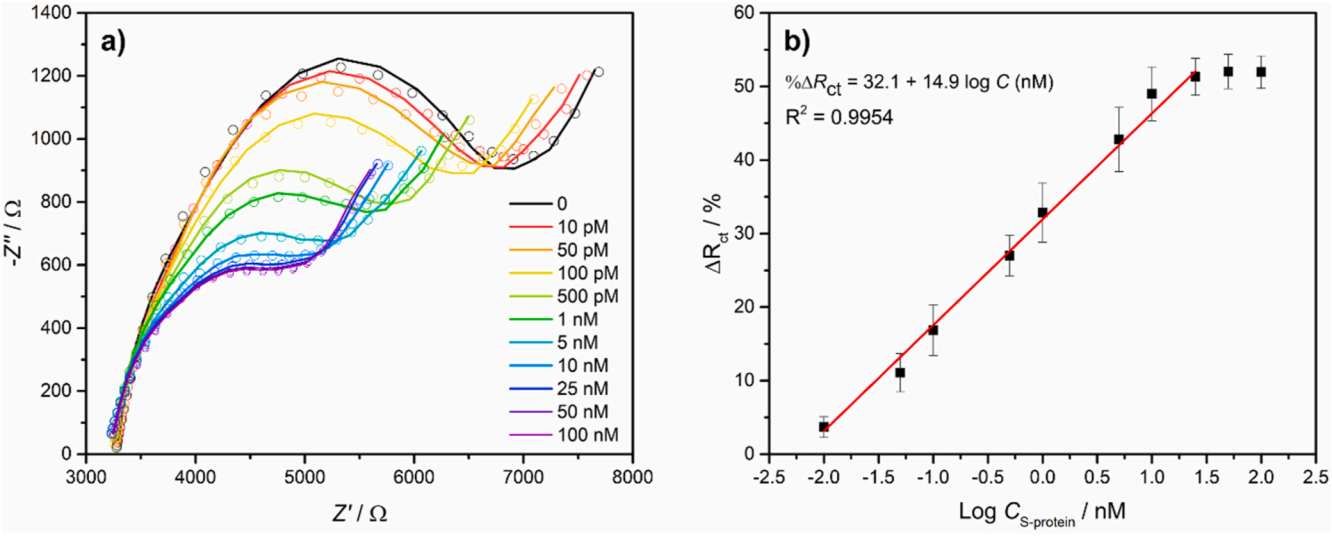

Fig. 3. a) Nyquist plots of the aptasensor response towards different concentrations of S-protein, recorded in PBS solution containing 5 mM $[Fe(CN)_6]^{3-/4-}$, solid lines correspond to the experimental data, while symbols correspond to the EIS data fitting, and b) calibration curve of the aptasensor with logarithmic S-protein concentration.

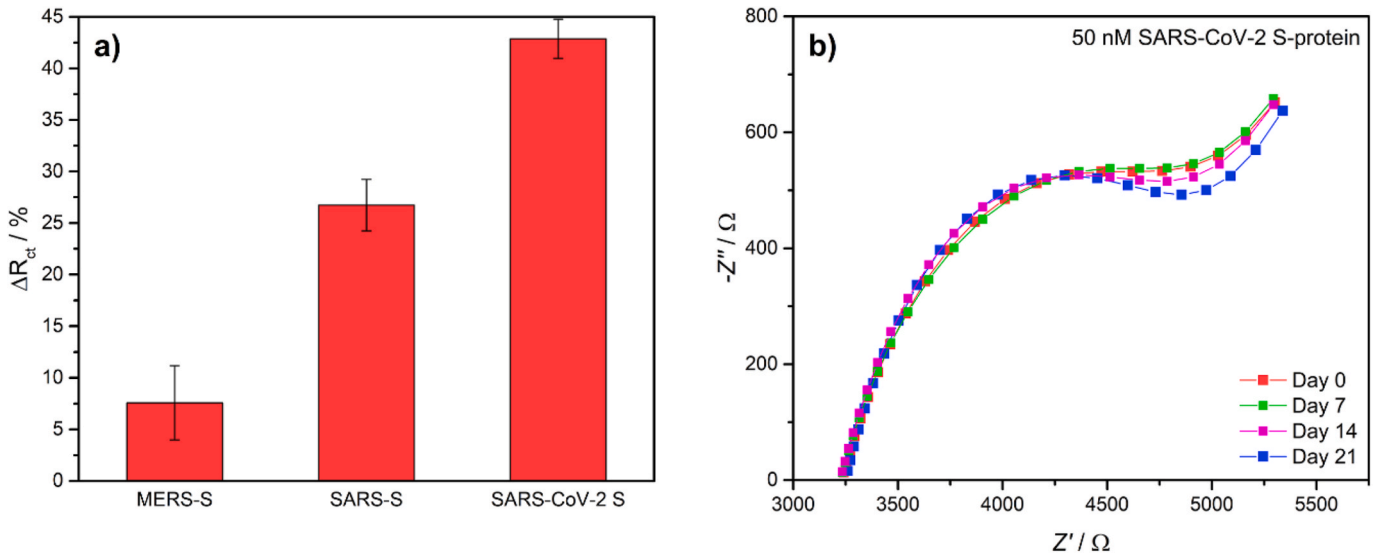

Fig. 4. a) Selectivity of the aptasensor studied with the S-proteins of MERS-CoV, SARS-CoV and SARS-CoV-2, and b) Impedimetric response obtained with 50 nM SARS-CoV-2 S-protein to evaluate the stability of the aptasensor after 3 weeks storing in BB.

deficient NL4-3 plasmid were also performed as control. The Nyquist plots and the relative response (%) are shown in Fig. 5. The fitting of the EIS data for the control measurement revealed a slightly higher R_{ct} in comparison with the response towards BB (no analyte). Since several different biomolecules are present in the $HIV_{NL4\text{-}3}$Env-luc sample, the observed response could be attributed to nonspecific binding of some of these species with the aptamer probe. On the other hand, after incubation with the SARS-CoV-2 pseudovirus, a lower R_{ct} was obtained with respect to the response towards BB. As shown in Fig. 3a, the presence of analyte in the aptamer probe induces a decrease in R_{ct}, therefore, the behavior of the aptasensor with the pseudovirus is consistent with the results obtained with purified S-protein, which indicates that the aptamer effectively captured the SARS-CoV-2 pseudovirus.

While viral-gene amplification techniques remain the standard for SARS-CoV-19 detection, and ICT tests are showing an increasing role as screening method due to their ease of use, the clear limitations, such as the inaccessible and costly RT-PCR machines (Abdalhamid et al., 2020) and the ICT tests being consistent only during the second week after infection (Pegoraro et al., 2021) are substantial barriers that setback a successful deconfinement and delay the end of the pandemic. On the other hand, the electrochemical aptasensor developed in this work was fabricated on a miniaturized, low-cost platform using widely available techniques and equipment, and it offers the possibility of early COVID-19 diagnosis by detecting the S-protein present in the SARS-CoV-2. This approach makes it possible to reproduce it in practically any bioelectrochemistry laboratory and even provides the feasibility of mass production in adequate facilities, although admittedly, the next phase (clinical testing) with groups of patients potentially infected with SARS-CoV-2 is necessary. In addition, the aptasensor can be used directly in a miniaturized, low-cost potentiostat coupled to a smartphone (Ainla et al., 2018), which adds to the user-friendly characteristics of this biosensor. The use of smartphones is an encouraging horizon for the miniaturized detection of SARS-CoV-2. Coupling the present biosensor with a smartphone would enable real-time fast detection of SARS-CoV-2 S-protein directly on the smartphone's screen, thus being a promising tool to complement or even replace existing SARS-CoV-19 detection methods.

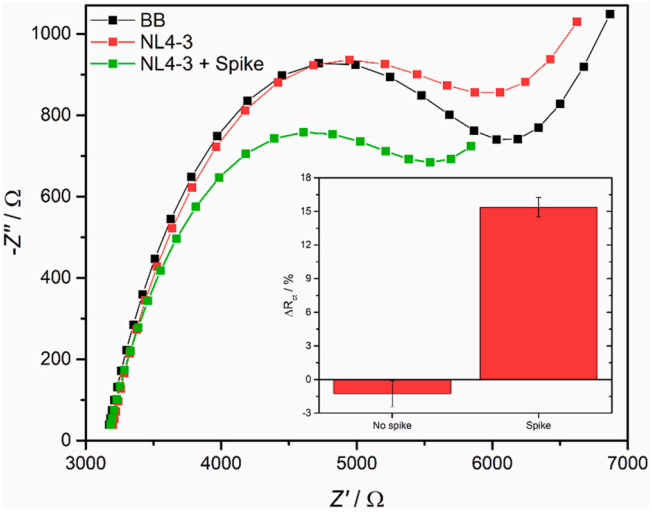

Fig. 5. Impedimetric response of the aptasensor towards the $HIV_{NL4\text{-}3}$Env-luc and the $HIV_{NL4\text{-}3}$Env-luc + S-protein pseudovirus. The inset is the percentage change in charge transfer resistance calculated from the EIS data.

4. Conclusions

In the present work, an aptamer-based impedimetric biosensor for detection of SARS-CoV-2 S-protein was successfully developed using a AuNPs-modified SPCE platform and an aptamer targeting the RBD of the SARS-CoV-2. The physicochemical characterization confirmed that the disulfide-modified aptamer was homogeneously immobilized on the surface of the AuNPs, which allowed the probe to capture S-protein atop practically all the AuNPs-modified surface, as revealed by the PiFM mapping imaging in the 1400 cm^{-1} region. The aptasensor demonstrated excellent sensing performance, as it required an analyte incubation time of 40 min to obtain a reliable reading, which is faster than the standard diagnostic tests, and it exhibited a LOD of 1.30 pM (66 pg/mL) for SARS-CoV-2 S-protein, lower than the LOD of PCR for the same analyte. The selectivity studies showed that the aptasensor is active to both SARS-CoV and SARS-CoV-2 S-proteins, however, the latter is more easily detected due to its more positively charged nature. Moreover, the aptasensor demonstrated consistent sensing activity when tested with a SARS-CoV-2 pseudovirus, which reaffirms the feasibility of practical application for COVID-19 detection. As a final remark, our biosensor was developed with practicality in mind, given the urgency for portable and fast detection methods. The use of screen-printed electrodes with a proven aptamer allows a reliable and straightforward application,

bringing up the possibility of using a hand-held potentiostat connected to a smartphone. By implementing a straightforward fabrication method, our device has a greater potential to be reproduced in most facilities, which is favorable in case of an eventual mass production.

CRediT authorship contribution statement

Juan Carlos Abrego-Martinez: Conceptualization, Methodology, Investigation, Formal analysis, Writing – original draft. **Maziar Jafari:** Investigation, Formal analysis, Writing – Reviewing and editing. **Siham Chergui:** Investigation. **Catalin Pavel:** Funding acquisition. **Diping Che:** Funding acquisition. **Mohamed Siaj:** Conceptualization, Resources, Supervision, Funding acquisition.

Declaration of competing interest

The authors declare that they have no known competing financial interests or personal relationships that could have appeared to influence the work reported in this paper.

Acknowledgements

We thank the Natural Sciences and Engineering Research Council of Canada (NSERC), the Canada Research Chairs program (CRC), Canada Foundation for Innovation (CFI) and NSERC-Alliance Covid-19 program. NanoQAM center at UQAM is gratefully acknowledged for all the characterization experiments. We thank Quebec Centre for Advanced Materials (QCAM).

Appendix A. Supplementary data

Supplementary data to this article can be found online at https://doi.org/10.1016/j.bios.2021.113595.

References

Abdalhamid, B., Bilder, C.R., Garrett, J.L., Iwen, P.C., 2020. J. Infec. Dev. Ctries. 14 (10), 1136.
Ainla, A., Mousavi, M.P., Tsaloglou, M.N., Redston, J., Bell, J.G., Fernández-Abedul, M. T., Whitesides, G.M., 2018. Anal. Chem. 90 (10), 6240–6246.
Ali, M.A., Hu, C., Jahan, S., Yuan, B., Saleh, M.S., Ju, E., Gao, S.J., Panat, R., 2021. Adv. Mater. 33 (7), 2006647.
Alpdagtas, S., Ilhan, E., Uysal, E., Sengor, M., Ustundag, C.B., Gunduz, O., 2020. APL Bioeng 4 (4), 041506.
Angerstein-Kozlowska, H., Conway, B., Hamelin, A., Stoicoviciu, L., 1986. Electrochim. Acta 31 (8), 1051–1061.
Bahadır, E.B., Sezgintürk, M.K., 2016. Artif. Cells. Nanomed. Biotechnol. 44 (1), 248–262.
Callaway, E., Ledford, H., 2021. Nature 590 (7844), 15–16.
Cerutti, F., Burdino, E., Milia, M.G., Allice, T., Gregori, G., Bruzzone, B., Ghisetti, V., 2020. J. Clin. Virol. 132, 104654.
Chen, Y.-T., Shao, S.-C., Lai, E.C.-C., Hung, M.-J., Chen, Y.-C., 2020. Crit. Care 24 (1), 1–4.
Cleri, F., Lensink, M.F., Blossey, R., 2020. ChemRxiv. https://doi.org/10.26434/chemrxiv.12696173.v1.
Darmostuk, M., Rimpelova, S., Gbelcova, H., Ruml, T., 2015. Biotechnol. Adv. 33 (6), 1141–1161.
De Assis, R.R., Jain, A., Nakajima, R., Jasinskas, A., Felgner, J., Obiero, J.M., Norris, P.J., Stone, M., Simmons, G., Bagri, A., 2021. Nat. Commun. 12 (1), 1–9.
Duan, L., Zheng, Q., Zhang, H., Niu, Y., Lou, Y., Wang, H., 2020. Front. Immunol. 11, 576622.
Eissa, S., Zourob, M., 2021. Anal. Chem. 93 (3), 1826–1833.
Elledge, S.K., Zhou, X.X., Byrnes, J.R., Martinko, A.J., Lui, I., Pance, K., Lim, S.A., Glasgow, J.E., Glasgow, A.A., Turcios, K., 2021. Nat. Biotechnol. 1–8.
Fan, L., Zhao, G., Shi, H., Liu, M., Li, Z., 2013. Biosens. Bioelectron. 43, 12–18.
Fischer, L.M., Tenje, M., Heiskanen, A.R., Masuda, N., Castillo, J., Bentien, A., Émneus, J., Jakobsen, M.H., Boisen, A., 2009. Microelectron. Eng. 86 (4–6), 1282–1285.
Fontanet, A., Autran, B., Lina, B., Kieny, M.P., Karim, S.S.A., Sridhar, D., 2021. Lancet 397 (10278), 952–954.
Fujigaki, H., Takemura, M., Osawa, M., Sakurai, A., Nakamoto, K., Seto, K., Fujita, T., Hata, T., Akiyama, H., Doi, Y., 2020. Heliyon 6 (9), e04929.
Gerges-Harb, J., Noureldine, H.A., Chedid, G., Eldine, M.N., Abdallah, D.A., Chedid, N.F., Nour-Eldine, W., 2020. Pathog. Dis. 78 (4), ftaa033.
Gilbert, G.L., 2020. Int. J. Epidemiol. 49 (3), 726–728.
Grujicic, D., Pesic, B., 2002. Electrochim. Acta 47 (18), 2901–2912.
Guarner, J., 2020. Am. J. Clin. Pathol. 153 (4), 420–421.
Hassanzadeh, K., Perez-Pena, H., Dragotto, J., Buccarello, L., Iorio, F., Pieraccini, S., Sancini, G., Feligioni, M., 2020. ACS Chem. Neurosci. 11 (15), 2361–2369.
Heiskanen, A.R., Spégel, C.F., Kostesha, N., Ruzgas, T., Emnéus, J., 2008. Langmuir 24 (16), 9066–9073.
Hezard, T., Fajerwerg, K., Evrard, D., Collière, V., Behra, P., Gros, P., 2012. Electrochim. Acta 73, 15–22.
Ho, L.S.J., Limson, J.L., Fogel, R., 2019. ACS Omega 4 (3), 5839–5847.
Hussain, A., Hasan, A., Babadaei, M.M.N., Bloukh, S.H., Chowdhury, M.E., Sharifi, M., Haghighat, S., Falahati, M., 2020. Biomed. Pharmacother. 130, 110559.
Inamdar, A., Mujawar, S., Sadale, S., Sonavane, A., Shelar, M., Shinde, P., Patil, P., 2007. Sol. Energy Mater. Sol. Cells 91 (10), 864–870.
Ji, T., Liu, Z., Wang, G., Guo, X., Lai, C., Chen, H., Huang, S., Xia, S., Chen, B., Jia, H., 2020. Biosens. Bioelectron. 166, 112455.
Kirtipal, N., Bharadwaj, S., Kang, S.G., 2020. Infect. Genet. Evol. 85, 104502.
Kucherova, A., Strango, S., Sukenik, S., 2020. BioRxiv. https://doi.org/10.1101/2020.10.29.361261.
Lee, J.-H., Choi, M., Jung, Y., Lee, S.K., Lee, C.-S., Kim, J., Kim, J., Kim, N.H., Kim, B.-T., Kim, H.G., 2021. Biosens. Bioelectron. 171, 112715.
Li, H., Burm, S.W., Hong, S.H., Abou Ghayda, R., Kronbichler, A., Smith, L., Koyanagi, A., Jacob, L., Lee, K.H., Shin, J.I., 2021. Yonsei Med. J. 62 (1), 1–11.
Long, C., Xu, H., Shen, Q., Zhang, X., Fan, B., Wang, C., Zeng, B., Li, Z., Li, X., Li, H., 2020. Eur. J. Radiol. 126, 108961.
Luan, J., Lu, Y., Jin, X., Zhang, L., 2020. Biochem. Biophys. Res. Commun. 526 (1), 165–169.
Mallamace, F., Corsaro, C., Mallamace, D., Vasi, S., Vasi, C., Dugo, G., 2015. Comput. Struct. Biotechnol. J. 13, 33–37.
Mavrikou, S., Moschopoulou, G., Tsekouras, V., Kintzios, S., 2020. Sensors 20 (11), 3121.
Mehennaoui, S., Poorahong, S., Jimenez, G.C., Siaj, M., 2019. Sci. Rep. 9 (1), 1–9.
Mehrotra, P., 2016. J. Oral Biol. Craniofac. Res. 6 (2), 153–159.
Neuman, B.W., Adair, B.D., Yoshioka, C., Quispe, J.D., Orca, G., Kuhn, P., Milligan, R.A., Yeager, M., Buchmeier, M.J., 2006. J. Virol. 80 (16), 7918–7928.
Oberhaus, F.V., Frense, D., Beckmann, D., 2020. Biosensors 10 (5), 45.
Parker, A.W., Quinn, S.J., 2013. Infrared spectroscopy of DNA. In: Roberts, G.C.K. (Ed.), Encyclopedia of Biophysics. Springer, Berlin, Heidelberg, pp. 1065–1074.
Pedersen, S.F., Ho, Y.-C., 2020. J. Clin. Invest. 130 (5), 2202–2205.
Peeri, N.C., Shrestha, N., Rahman, M.S., Zaki, R., Tan, Z., Bibi, S., Baghbanzadeh, M., Aghamohammadi, N., Zhang, W., Haque, U., 2020. Int. J. Epidemiol. 49 (3), 717–726.
Pegoraro, M., Militello, V., Salvagno, G.L., Gaino, S., Bassi, A., Caloi, C., Peretti, A., Bizzego, S., Poletto, L., Bovo, C., 2021. Eur. J. Clin. Microbiol. Infect. Dis. 40 (4), 897–900.
Polito, R., Musto, M., Temperini, M.E., Ballerini, L., Ortolani, M., Baldassarre, L., Casalis, L., Giliberti, V., 2021. Molecules 26 (4), 887.
Rouya, E., Cattarin, S., Reed, M., Kelly, R., Zangari, G., 2012. J. Electrochem. Soc. 159 (4), K97.
Shang, J., Ye, G., Shi, K., Wan, Y., Luo, C., Aihara, H., Geng, Q., Auerbach, A., Li, F., 2020. Nature 581 (7807), 221–224.
Shereen, M.A., Khan, S., Kazmi, A., Bashir, N., Siddique, R., 2020. J. Adv. Res. 24, 91–98.
Shrivastava, A., Gupta, V.B., 2011. Chronicles Young Sci. 2 (1), 21–25.
Smith, R., 2019. Am. J. Biomed. Sci. Res. 6 (2), 152–155.
Song, Y., Song, J., Wei, X., Huang, M., Sun, M., Zhu, L., Lin, B., Shen, H., Zhu, Z., Yang, C., 2020. Anal. Chem. 92 (14), 9895–9900.
Sun, M., Liu, S., Wei, X., Wan, S., Huang, M., Song, T., Lu, Y., Weng, X., Lin, Z., Chen, H., 2021. Angew. Chem. 60, 10266–10272.
Tahamtan, A., Ardebili, A., 2020. Expert Rev. Mol. Diagn. 20 (5), 453–454.
Tian, Y., Liu, H., Zhao, G., Tatsuma, T., 2006. J. Phys. Chem. B 110 (46), 23478–23481.
Tombelli, S., Minunni, M., Mascini, M., 2005. Biosens. Bioelectron. 20 (12), 2424–2434.
Udugama, B., Kadhiresan, P., Kozlowski, H.N., Malekjahani, A., Osborne, M., Li, V.Y., Chen, H., Mubareka, S., Gubbay, J.B., Chan, W.C., 2020. ACS Nano 14 (4), 3822–3835.
Wood, B.R., 2016. Chem. Soc. Rev. 45 (7), 1980–1998.
Wouters, O.J., Shadlen, K.C., Salcher-Konrad, M., Pollard, A.J., Larson, H.J., Teerawattananon, Y., Jit, M., 2021. Lancet 397 (10278), 1023–1034.
Wrapp, D., Wang, N., Corbett, K.S., Goldsmith, J.A., Hsieh, C.-L., Abiona, O., Graham, B. S., McLellan, J.S., 2020. Science 367 (6483), 1260–1263.
Yakoh, A., Pimpitak, U., Rengpipat, S., Hirankarn, N., Chailapakul, O., Chaiyo, S., 2021. Biosens. Bioelectron. 176, 112912.
Yüce, M., Filiztekin, E., Özkaya, K.G., 2021. Biosens. Bioelectron. 172, 112752.
Zeng, L., Li, Y., Liu, J., Guo, L., Wang, Z., Xu, X., Song, S., Hao, C., Liu, L., Xin, M., 2020. Mater. Chem. Front. 4 (7), 2000–2005.
Zhao, H., Liu, F., Xie, W., Zhou, T.-C., OuYang, J., Jin, L., Li, H., Zhao, C.-Y., Zhang, L., Wei, J., 2021. Sensor. Actuator. B Chem. 327, 128899.
Zhu, N., Zhang, D., Wang, W., Li, X., Yang, B., Song, J., Zhao, X., Huang, B., Shi, W., Lu, R., 2020. N. Engl. J. Med. 382 (8), 727–733.